# Improving Microgrid Low-Voltage Ride-Through Capacity Using Neural Control

Larbi Djilali, Edgar N. Sanchez, Fernando Ornelas-Tellez, Alberto Avalos, and Mohammed Belkheiri

***Abstract*—In this article, a neural sliding-mode linearization controller is proposed to regulate the generated active and reactive power for each distributed energy resource in a microgrid. The developed controller is based on recurrent high-order neural network identification, trained online with an extended Kalman filter learning algorithm. Based on such neural identification, adequate models of the microgrid generation units are obtained even in the presence of grid disturbances, which helps the proposed controller to reject disturbances, to ensure stability, and to operate the renewable energy sources under different grid scenarios. The proposed microgrid is composed of a wind power system, a solar power system, a battery bank, and a load demand. In addition, the microgrid under study is interconnected to an IEEE nine-bus system. The whole system is simulated in real time using the Opal-RT (OP5600) simulator. Real-time simulation results illustrate the effectiveness of the proposed control scheme to achieve trajectory tracking of the distributed energy resources active and reactive power even in the presence of grid disturbances.**

***Index Terms*—Distributed energy resources (DERs), grid-connected microgrid, low-voltage ride-through (LVRT), neural network identification, real-time simulation, sliding mode.**

## NOMENCLATURE

| | |
|---|---|
| $x_k, \chi_k$ | Real and estimated state vector. |
| $u_k, y_k$ | Input vector and output vector. |
| $w_i, \varpi_i$ | Neural identifier adaptive and fixed weights. |
| $v_c(x_k)$ | Decoupled control part. |
| $v_{\text{eqn}}(x_k)$ | Equivalent control. |
| $v_{\text{stn}}(x_k)$ | Stabilizing term. |
| $s_{n,k}$ | Sliding surface. |
| $U_{\text{dc},k}, \hat{U}_{\text{dc},k}$ | Real and estimated dc-link voltage. |
| $i_{gd,k}, i_{gq,k}$ | Grid $d$–$q$ currents. |
| $u_{gcd,k}, u_{gcq,k}$ | Grid-side converter $d$–$q$ inputs. |
| $\hat{i}_{gd,k}, \hat{i}_{gq,k}$ | Estimated grid $d$–$q$ currents. |
| $i_{rd,k}, i_{rq,k}$ | Rotor $d$–$q$ currents. |
| $\hat{i}_{rd,k}, \hat{i}_{rq,k}$ | Estimated rotor $d$–$q$ currents. |
| $u_{rd,k}, u_{rq,k}$ | Rotor-side converter $d$–$q$ inputs. |
| $U_{\text{dcpv},k}, I_{\text{pv}}$ | Boost output voltage and current. |
| $U_{\text{pv},k}$ | Output solar panel voltage. |
| $\hat{U}_{\text{dcpv},k}, \hat{I}_{\text{pv},k}$ | Estimated boost output voltage and current. |
| $u_{\text{pvbo},k}$ | Boost input. |
| $i_{d,k}, i_{q,k}$ | Solar panel inverter $d$–$q$ currents. |
| $\hat{i}_{d,k}, \hat{i}_{q,k}$ | Estimated SPS $d$–$q$ currents. |
| $u_{d,k}, u_{q,k}$ | Solar inverter $d$–$q$ inputs. |
| $U_{\text{dcbtt},k}, I_{\text{btt}}$ | Buck–boost voltage and current. |
| $U_{\text{btt},k}$ | Battery bank voltage. |
| $\hat{U}_{\text{dcbtt},k}, \hat{I}_{\text{btt},k}$ | Estimated buck–boost voltage and current. |
| $u_{c,k}$ | Buck–boost input. |

## I. INTRODUCTION

NOWADAYS, the penetration of generated power using renewable energy sources into the utility grid has been growing continuously. In order to reach better exploitation of the renewable energy, which is generated from different distributed energy resources (DERs), the microgrid concept is being developed [1]. A microgrid is a low-to-medium-voltage distribution network, which includes alternative sources like wind power systems (WPSs), solar power systems (SPSs), energy storage devices as battery bank (BB), local loads, and power electronic devices among other electrical components. The purpose of using appropriate power converters is to facilitate the DER connection to the main grid, to guarantee high generated power quality, and to control power flows [2].

Because of disturbances and voltage fluctuations, inappropriate effects can be produced and might affect the operation of DERs installed into microgrids; those disturbances actually present big challenges for microgrid control [3]. In the past, DERs were disconnected during grid disturbances [4]. This discontinuity in power generation might affect stability and reliability of the whole network [5]. Taking into account high penetration of renewable energy generation into medium- and high-voltage networks, modern grid codes enforce DERs to have low-voltage ride-through (LVRT) capacity, which is the capability of a specific electric generator to stay connected to the main grid in the presence of low voltage for a short period; additionally, the installed local controllers should warranty microgrid transient stability and guarantee the transient stability to enhance resilience of microgrid operations.

Manuscript received February 27, 2019; revised September 12, 2019; accepted October 12, 2019. This work was supported by the Consejo Nacional de Ciencia y Tecnología, Mexico, under Projects 257200 and CB-222760. *(Corresponding author: Larbi Djilali.)*

L. Djilali is with Automatic Control Laboratory, CINVESTAV Guadalajara, Zapopan 45019, Mexico, and also with Telecommunications, Signals and Systems Laboratory, University Amar Telidji, Laghouat 3000, Algeria (e-mail: ldjilali@gdl.cinvestav.mx).

E. N. Sanchez is with Automatic Control Laboratory, CINVESTAV Guadalajara, Zapopan 45019, Mexico (e-mail: sanchez@gdl.cinvestav.mx).

F. Ornelas-Tellez and A. Avalos are with the Faculty of Electrical Engineering, Universidad Michoacana de San Nicolás de Hidalgo, Morelia 58030, Mexico (e-mail: fornelas@umich.mx; javalos65@gmail.com).

M. Belkheiri is with Telecommunications, Signals and Systems Laboratory, University Amar Telidji, Laghouat 3000, Algeria (e-mail: m.belkheiri@lagh-univ.dz).

Digital Object Identifier 10.1109/JSYST.2019.2947840

In the literature, different methodologies using hardware devices and/or modified control schemes have been developed in order to accomplish the LVRT requirements. For hardware components, there are different shunt/series devices included in DER electrical configurations, such as protection devices/circuits activated during transient, and there are also reactive power injecting devices in order to compensate voltage dips [6]. These solutions are effective but make the control scheme more complex and increase the total cost and power losses [7]. To overcome hardware solutions drawbacks, different control strategies are adopted to achieve LVRT capacity requirements. The most known controllers, which are used to regulate DER dynamics, are the conventional proportional–integral (PI) and the proportional-resonance controllers [8], [9]. To develop those controllers for LVRT enhancement, a decomposition process is needed, which makes control implementation more complex [10]; in addition, these classical controllers are inappropriate for trajectory tracking control, which is a required task for DER energy generation [11]. Another control technique that is widely used for microgrid applications is the droop control [1], [12], which is usually implemented using voltage and current control loops or power and current control ones in a cascade configuration [13]. In [1], an LVRT control scheme, which improves power quality during abnormal grid conditions, is developed, where a cascade voltage and current control loop and a modified droop technique are used to perform primary- and secondary-level control; the latter controls the reactive power injection. In [14], a hierarchical control that consists of primary and secondary layers is proposed, where the primary layer based on the droop controller is in charge of power regulation, while the secondary layer consists of a dynamics consensus algorithm, which is responsible of the LVRT operation of the microgrid. The droop method can be implemented without communication links between microgrid subsystems, which improves reliability; its drawbacks are largely discussed in the literature as [15]. In addition, LVRT capacity in DERs connected to microgrid-based droop control has not been adequately addressed [1], [15]. Moreover, big efforts are being made to develop an efficient-LVRT-scheme-based control to ensure microgrid stability in the presence of grid disturbances.

Recently, technology advances have forced control engineers to deal with complex systems, which include unknown dynamics, strong interconnection terms, and disturbances [16]. Then, conventional control techniques are unsuccessful to provide an effective solution to control this class of systems. Neural networks have the potential for implementing nonlinear system identification and control due to their capabilities to approximate complex systems and to improve control scheme performances [17]. In [18], a combinational scheme of neural-network-based PI controller for the distribution static synchronous compensator and crowbar is proposed to enhance doubly fed induction generator (DFIG) transient stability in the presence of asymmetrical faults; the included results illustrate the effectiveness of the proposed technique; however, additional devices are needed. In [19], a neural-network-based PI controller and a classical one are compared regarding the impact of each controller on the LVRT behavior of the DFIG under different load models. In [20], an intelligent controller based on the Takagi–Sugeno–Kang-type probabilistic fuzzy neural network is developed for the reactive and active power control of a grid connected photovoltaic system in the presence of grid faults; the proposed controller allows us to regulate the reactive power to a new desired value in order to fulfill the LVRT requirements. In [21], a fault detection and identification based on voltage indicator analysis using a neural network is developed for enhancing the LVRT capacity of the DFIG. The results obtained in [19]–[21] illustrate the effectiveness of the proposed schemes; however, they do not consider a large-scale power system with more DER components.

This article extends the results of [22], where the proposed neural sliding-mode linearization (NSML) control was applied to regulate the active and reactive power of DERs under normal grid conditions. In this article, the proposed scheme is used to control: 1) the WPS-generated power based on a DFIG; 2) the SPS-injected power, which is linked to the microgrid through a boost converter and an inverter; and 3) the BB-delivered power, which is connected to the microgrid via a buck–boost converter and an inverter. The microgrid system is interconnected to an IEEE nine-bus test system to evaluate its connection performance and response under grid disturbances.

This article aims to improve the LVRT capacity of DERs in the presence of grid disturbances by means of the following.

1) A controller based on a recurrent high-order neural network (RHONN) identifier, trained online by an extended Kalman filter (EKF), is proposed for each DER. The proposed neural identifier helps to estimate the dynamics of each microgrid DER even in the presence of parameter variations and/or grid disturbances.
2) The obtained neural model is used to synthesize the neural linearization control part of the proposed scheme, which is utilized to linearize the system and to reject perturbations caused by parameter changes and/or grid disturbances.
3) A sliding-mode controller is used to achieve the trajectory tracking and to eliminate identification errors.

These errors are very small as addressed in [17], resulting in a large reduction of the sliding-mode chattering phenomena. By using the proposed control scheme, the LVRT capacity of DERs is enhanced in the presence of grid disturbances, which are incepted in both sides of the microgrid and/or utility grid (in this case, IEEE nine-bus test system). At the same time, stability is ensured for all DER components.

The rest of this article is organized as follows. In Section II, mathematical preliminaries are presented. In Section III, the proposed microgrid and the IEEE nine-bus test system are described. The proposed neural controller is developed in Section IV. Real-time simulation results of the proposed control strategy are discussed in Section V. Finally, conclusion is provided in Section VI.

## II. MATHEMATICAL PRELIMINARIES

### A. *Neural Identification*

Consider the following nonlinear system [11]:

$$x_{k+1} = f(x_k) + B(x_k)u(x_k) + d(x_k) \tag{1}$$

$$y_k = h(x_k) \tag{2}$$

where $k \in \mathbb{Z}^+ \cup \{0\}$ denotes the discrete time, with $\mathbb{Z}^+$ being the set of positive integers, $x_k \in \Re^n$ is the state vector of the system, $u_k \in \Re^m$ is the input vector, $y_k \in \Re^p$ is the output vector to be controlled, and the functions $f(\bullet)$, $B(\bullet)$, $h(\bullet)$, and $d(\bullet)$ are smooth and bounded vector fields. Note that this article proposes the modeling and control design in discrete time, as well as the application, for which well-defined methodologies and algorithms can be implemented in real time. The selection of the neural identifier structure is arbitrary, but it considers the structure of system (1), (2). There are different considerations to be taken into account for the neural network design, such as maintaining properties like controllability, improving robustness in the presence of internal disturbances as well as external ones, and solving control implementation problems caused by couplings among subsystems, inputs, and outputs [17]. Using a series–parallel configuration, the proposed neural identifier for system (1) is given by [17]

$$\chi_{i,k+1} = w_i^T \phi_i(x_k) + \varpi_i^T \varphi_i(x_k, u_k) \tag{3}$$

where $\chi_{i,k}$ is the state of the $i$th neuron, which identifies the $i$th component of $x_k$, $w_i \in \Re^{L_i}$ are adjustable weights of the neural identifier, $\varpi_i$ are the fixed ones for the control matrix, $\phi_i \in \Re^{L_i}$ is a smooth vector function defined as $\phi_i(\bullet) = [\phi_{i,1}(.), \ldots, \phi_{i,L}(.)]^T \in \Re^{L_i}$ and $L_i$ is the connection number, such as each component is given as $\phi_{i,j}(\bullet) = \phi_{i,1}(S(x_{1,k}), \ldots, S(x_{n,k}))^T$, and $\varphi_i$ is a linear function of the states or inputs. The function $S(\bullet)$ is an activation function; it is selected as a hyperbolic tangent function [17]. In order to attain identification objectives, the EKF-based algorithm is selected to train the proposed neural identifier [17], as follows:

$$K_{i,k} = P_{i,k} H_{i,k} \left[ R_{i,k} + H_{i,k}^T P_{i,k} H_{i,k} \right]^{-1} \tag{4}$$

$$w_{i,k+1} = w_{i,k} + \eta_i K_{i,k} e_{i,k} \tag{5}$$

$$P_{i,k+1} = P_{i,k} - K_{i,k} H_{i,k}^T P_{i,k} + Q_{i,k} \tag{6}$$

$$e_{i,k} = x_{i,k} - \chi_{i,k}, \quad i = 1, 2, \ldots, n \tag{7}$$

where $e_i \in R$ is the identification error of each state, $P_i \in R^{L_i \times L_i}$ is the covariance matrix of prediction errors, $w_i \in R^{l_i}$ is the adjustable weights vector, $\eta_i$ is a constant parameter, $K_{i,k} \in R^{L_i \times m}$ is the Kalman gain matrix, $Q_{i,k} \in R^{L_i \times L_i}$ is the covariance matrix associated with the state noise, $R_{i,k} \in R^{m \times m}$ is the covariance matrix associated with the measurement noise, and $H_i \in R^{L_i \times m}$ is a matrix containing the derivative of the neural network states $x_i$ with respect to each neural weight.

### *B. NSML Control*

In this section, the NSML controller is synthesized. Taking into consideration neural identification properties, such as the capability to absorb disturbances, the proposed neural model (3) for system (1), (2) is rewritten as

$$\chi_{k+1} = \hat{f}(x_k) + \hat{B} u(x_k) \tag{8}$$

$$\hat{y}_k = \hat{h}(x_k) \tag{9}$$

where $\chi_k \in \Re^n$ is the estimated state vector, $\hat{y}_k \in \Re^p$ is the estimated output vector to be controlled, $\hat{B}$ is the control matrix composed by the fixed weights, and the vector $\hat{f}(\bullet)$, and $\hat{h}(\bullet)$ are smooth and bounded vector fields. By considering the discrete-time separation principle [23], which states that the identifier and controller can be independently synthesized, the NSML controller is established as follows.

*Theorem 1:* For the system (8), (9), the NSML control law

$$u(x_k) = -\hat{B}^{-1} \hat{f}(x_k) + v(x_k) \tag{10}$$

allows us to use the discrete-time sliding-mode control (DTSMC) methodology to define $v(x_k)$ in order to ensure that the respective sliding manifold is ultimately bounded, achieving system outputs converging toward their respective desired values.

The proposed control law (10) is composed of two parts: 1) the neural linearization control part, which is expressed by $(-\hat{B}^{-1} \hat{f}(x_k))$ with a negative sign to exactly eliminate the term $\hat{f}(x_k)$ in order to linearize (8) and 2) the decoupled control part $v(x_k)$, which is determined by a DTSMC as follows. Equation (9) at $k+1$ is calculated as follows:

$$\hat{y}_{k+1} = \chi_{k+1} = \hat{f}(x_k) + \hat{B} u(x_k). \tag{11}$$

The matrix $\hat{B}$ is invertible because it is composed of the fixed weights; the neural linearization control part is calculated by (10). Substituting (10) into (8), the decoupled linear system is obtained as

$$\hat{y}_{k+1} = v(x_k) \tag{12}$$

with $v(x_k)$ determined by means of the DTSMC [24] as

$$v(x_k) = \begin{cases} v_c(x_k), & \text{if } \|v_c(x_k)\| \le u_0 \\ u_0 \frac{v_{\text{eqn}}(x_k)}{\|v_{\text{eqn}}(x_k)\|}, & \text{if } \|v_c(x_k)\| > u_0 \end{cases} \tag{13}$$

where $\| v(x_k) \| < u_0, u_0 > 0$ is the bound of the control signal, and $v_c(x_k) = v_{\text{eqn}}(x_k) + v_{\text{stn}}(x_k)$, where $v_{\text{eqn}}(x_k)$ is the equivalent control and $v_{\text{stn}}(x_k)$ is a stabilizing term. The sliding-mode surface is selected as follows:

$$s_{n,k} = \chi_k - x_{\text{ref},k} \tag{14}$$

with $x_{\text{ref},k}$ being the reference signal to be tracked. The $s_{n,k}$ expression at $k+1$ is obtained as

$$s_{n,k+1} = v(x_k) - x_{\text{ref},k+1}. \tag{15}$$

Then, the equivalent control is calculated by evaluating $s_{n,k+1} = 0$ as follows:

$$v_{\text{eqn}}(x_k) = x_{\text{ref},k+1}. \tag{16}$$

Using (16) in (15), the sliding surface $s_{n,k} = 0$ is reached in one sample time. The stabilizing term is calculated as

$$v_{\text{stn}}(x_k) = -k_n s_{n,k} \tag{17}$$

where $k_n$ is the Schur matrix [25]. The corresponding proof of Theorem 1 is included in the Appendix.

## III. CONSIDERED MICROGRID

The considered microgrid is presented in Fig. 1. It is composed of an WPS based on the DFIG, whose rotor is linked to the microgrid through a back-to-back converter, while its stator is directly connected to the microgrid; an SPS linked to the microgrid through two converters: a boost converter and an inverter; a

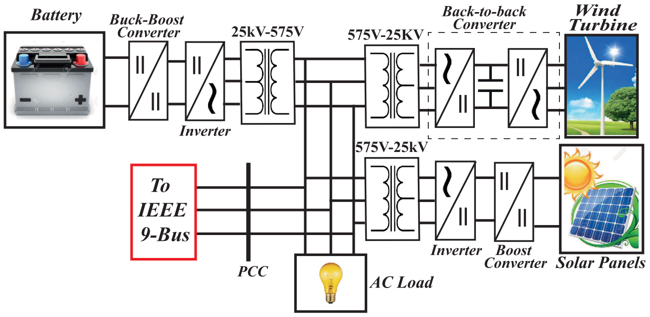

Fig. 1. Microgrid electrical structure.

BB coupled to the microgrid via a series-connected buck–boost converter to an inverter; and a load demand. In addition, this microgrid is linked through bus nine to an IEEE nine-bus test system, which consists of nine buses, four electric synchronous generators with IEEE type-1 exciters, three ac electric loads, six transmission lines, and five electric transformers. For more details about the IEEE nine-bus test system see [26] and [27]. The structure of this IEEE nine-bus system is presented in Fig. 2.

## IV. MICROGRID NEURAL CONTROLLERS

RHONN identifiers are proposed for the microgrid components to improve robustness of the proposed control scheme in the presence of parameter variations and/or grid disturbances; it is assumed that all the state variables are measured. The design of the RHONN identifier takes into account the following considerations.

1) The proposed neural identifier for each DER should have an appropriate structure considering state and input vectors.
2) The proposed neural identifier structure should be designed using a minimum number of sensors in order to reduce costs.
3) Based on the neural identifier capability to absorb disturbances, the interconnection terms as well as disturbances are not included in the proposed neural models.
4) The proposed neural identifier should be selected to reduce coupling between the control axes and to simplify the controller design and implementation.

### *A. WPS Neural Controller*

Regarding the mechanical part, it is assumed that the DFIG is operated at its synchronous speed.

*1) DC Link:* The objective of this controller is to force the voltage at the dc-link output to track desired values and at the same time to track the microgrid power factor reference. The respective RHONN identifier is proposed as [22]

$$\chi_{1,k+1} = \hat{f}_1(x_{1,k}) + \hat{B}_1 u_1(x_{1,k}) \tag{18}$$

$$\hat{y}_{1,k} == \hat{h}_1(x_{1,k}) \tag{19}$$

where $x_{1,k} = [U_{\mathrm{dc},k}\ i_{gd,k}\ i_{gq,k}]^T$ is the state vector, which is the dc voltage at the dc link, $i_{gd,k}$ and $i_{gq,k}$ are the grid $d$ and $q$ currents, respectively, $\chi_{1,k} = [\hat{U}_{\mathrm{dc},k}\ \hat{i}_{gd,k}\ \hat{i}_{gq,k}]^T$ is the vector estimated by the neural identifier, $u_1 = [u_{gcd,k}\ u_{gcq,k}]^T$ is the control vector, which is constituted by the grid-side converter voltages, $\hat{y}_1 = [\hat{h}_{11}(x_{1,k})\ \hat{h}_{12}(x_{1,k})\ \hat{h}_{13}(x_{1,k})]^T = [\hat{U}_{\mathrm{dc},k}\ \hat{i}_{gd,k}\ \hat{i}_{gq,k}]^T$ is the output vector to be controlled, $\hat{B}_1 = \mathrm{diag}[\varpi_{1,2}, \varpi_{1,3}]$, and $\hat{f}_1(x_{1,k}) = [\hat{f}_{11}(x_{1,k})\ \hat{f}_{12}(x_{1,k})\ \hat{f}_{13}(x_{1,k})]$, where

$$\hat{f}_{11}(x_{1,k}) = w_{11}S(U_{\mathrm{dc},k}) + w_{12}S(U_{\mathrm{dc},k})S(i_{gq,k}) + \varpi_{1,1}i_{gd,k}$$

$$\hat{f}_{12}(x_{1,k}) = w_{21}S(i_{gd,k}) + w_{22}S(i_{gq,k}) + w_{23}S(U_{\mathrm{dc},k})$$

$$\hat{f}_{13}(x_{1,k}) = w_{31}S(i_{gq,k}) + w_{32}S(i_{gd,k}).$$

From (18) and (19), the dc voltage is controlled by the grid $d$ currents. Using Theorem 1, the dc voltage neural linearization control part is calculated as

$$i_{gd,k} = \frac{-1}{\varpi_{1,1}}\hat{f}_{11}(x_k) + v_{1,1,k} \tag{20}$$

with $\varpi_{1,1} \neq 0$ a fixed weight and $v_{1,1,k}$ the dc-voltage-decoupled control such that a DTSMC is used to define it, as shown in Theorem 1, where $v_{\mathrm{eqn}_{1,1}}$ is the equivalent control defined as

$$v_{\mathrm{eqn}_{1,1}} = U_{\mathrm{dcref},k+1} \tag{21}$$

where $U_{\mathrm{dcref},k}$ is the dc voltage desired value. The stabilizing term $v_{\mathrm{stn}_{1,1}}$ is defined as

$$v_{\mathrm{stn}_{1,1}} = -k_{1,1}s_{1n,1,k} \tag{22}$$

where $s_{1n,1,k}$ is the dc voltage sliding surface defined as $s_{1n,1,k} = U_{\mathrm{dcref},k} - \hat{U}_{\mathrm{dc},k}$.

The dc voltage control law $i_{gd,k}$ determines the grid $d$ current desired values (20). In order to define the grid $q$ reference, the following expression is used:

$$i_{\mathrm{gqref},k} = -i_{gd,k}\frac{\sqrt{1 - f_{\mathrm{gref}}^2}}{f_{\mathrm{gref}}} \tag{23}$$

where $f_{\mathrm{gref}}$ is the grid power factor desired value. Using Theorem 1, the grid current neural linearization control part is obtained from $\hat{h}_{12}(x_{1,k})$ and $\hat{h}_{13}(x_{1,k})$ at $k+1$ as

$$\begin{bmatrix} u_{gcd,k} \\ u_{gcq,k} \end{bmatrix} = \hat{B}_1^{-1}\begin{bmatrix} -\hat{f}_{12}(x_k) \\ -\hat{f}_{13}(x_k) \end{bmatrix} + \begin{bmatrix} v_{1,2,k} \\ v_{1,3,k} \end{bmatrix} \tag{24}$$

where $v_{1,2,k}$ and $v_{1,3,k}$ are the grid-current-decoupled control parts, which are defined as described in Section II [see (12)–(17)] such that the sliding surfaces of the grid currents are defined as $s_{1n,2,k} = i_{\mathrm{gdref},k} - \hat{i}_{gd,k}$ and $s_{1n,3,k} = i_{\mathrm{gqref},k} - \hat{i}_{gq,k}$.

*2) DFIG:* The purpose of this controller is to track the desired dynamics of the stator active and reactive power through the control of the rotor $d$–$q$ currents; their neural identifier is selected as follows:

$$\chi_{2,k+1} = \hat{f}_2(x_{2,k}) + \hat{B}_2 u_2(x_{2,k}) \tag{25}$$

$$\hat{y}_{2,k} == \hat{h}_2(x_{2,k}) \tag{26}$$

where $x_{2,k} = [i_{rd,k}\ \ i_{rq,k}]^T$ is the DFIG rotor currents state vector, $\chi_2 = [\hat{i}_{rd,k}\ \ \hat{i}_{rq,k}]^T$ is the vector estimated by the

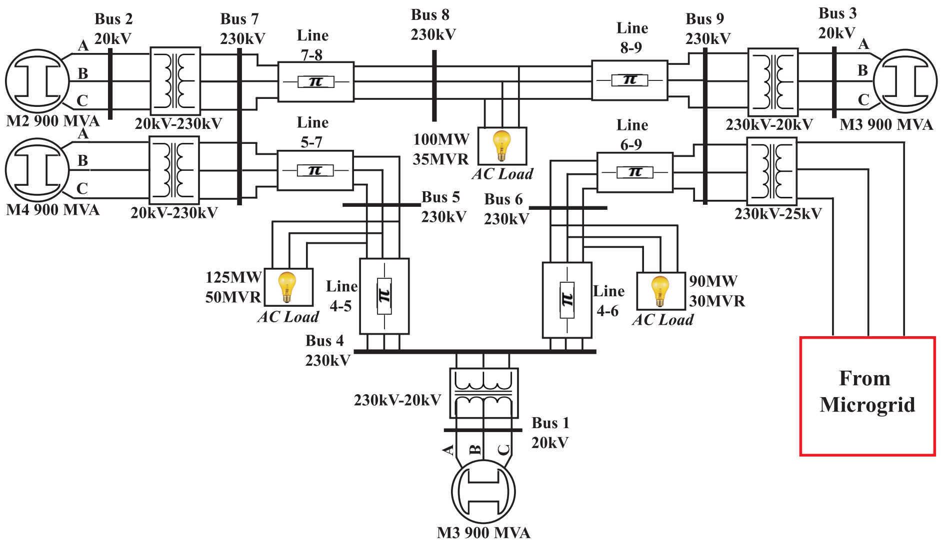

Fig. 2. IEEE nine-bus electric structure.

neural identifier, $u_{2,k} = [u_{rd,k}\ u_{rq,k}]^T$ is the control vector, $\hat{y}_2 = [\hat{h}_{21}(x_{2,k})\ \ \hat{h}_{22}(x_{2,k})]^T = [\hat{i}_{rd,k}\ \ \hat{i}_{rq,k}]^T$ is the output vector to be controlled, $\hat{B}_2 = \text{diag}[\varpi_{2,1}, \varpi_{2,2}]$, and $\hat{f}_2(x_{2,k}) = [\hat{f}_{21}(x_{2,k})\ \ \hat{f}_{22}(x_{2,k})]^T$ is as

$$\begin{aligned}\hat{f}_{21}(x_{2,k}) &= w_{11,k}S(i_{rd,k}) + w_{12,k}S(i_{rd,k})S(i_{rq,k})\\ &\quad + w_{13,k}S(i_{rq,k})\\ \hat{f}_{22}(x_{2,k}) &= w_{21,k}S(i_{rq,k}) + w_{22,k}S(i_{rd,k})S(i_{rq,k})\\ &\quad + w_{23,k}S(i_{rd,k}).\end{aligned}$$

In order to design the NSML controller for the stator active and reactive power, the same steps as explained in Theorem 1 are followed. The neural linearization control is obtained as

$$\begin{bmatrix} u_{rd,k} \\ u_{rq,k} \end{bmatrix} = \hat{B}_2^{-1} \begin{bmatrix} -\hat{f}_{23}(x_k) \\ -\hat{f}_{24}(x_k) \end{bmatrix} + \begin{bmatrix} v_{2,1,k} \\ v_{2,2,k} \end{bmatrix} \tag{27}$$

where $v_{2,1,k}$ and $v_{2,2,k}$ are the rotor-decoupled control parts, which are defined as described in Section II [see (12)–(17)], such that the sliding surfaces of the rotor current, $s_{2n,1,k}$ and $s_{2n,2,k}$, are defined as $s_{2n,1,k} = i_{\text{rdref},k} - \hat{i}_{rd,k}$, and $s_{2n,2,k} = i_{\text{rqref},k} - \hat{i}_{rq,k}$, respectively. The desired value of the rotor currents is obtained by using the following expressions:

$$i_{\text{rdref},k} = k_{dq}e_{q,k} + k_{iq}\frac{t_s}{z-1}e_{q,k} \tag{28}$$

where $e_{q,k} = Q_{\text{sref},k} - Q_{s,k}$ is the error of the desired and real dynamics of the stator reactive power, $k_{dq}$ and $k_{iq}$ are the proportional and integral controller gains, respectively, and $t_s$ is the sample time, and

$$i_{\text{rqref},k} = k_{dp}e_{p,k} + k_{ip}\frac{t_s}{z-1}e_{p,k} \tag{29}$$

where $e_{p,k} = P_{\text{sref},k} - P_{s,k}$ is the error of the desired and real trajectory of the stator active power.

### *B. SPS Neural Controller*

*1) Boost Converter:* The objective is to force the dc voltage at the output of the boost converter to keep its desired constant value. In order to do so, the control scheme is composed of two controllers in cascade. The first one is used to generate the reference of the boost converter output current, and the second one is utilized to track the obtained current reference. The proposed RHONN identifier for this converter is selected as follows:

$$\chi_{3,k+1} = \hat{f}_3(x_{3,k}) + \hat{B}_3u_3(x_{3,k}) \tag{30}$$

$$\hat{y}_{3,k} == \hat{h}_3(x_{3,k}) \tag{31}$$

where $x_{3,k} = [U_{\text{dcpv},k}\ \ I_{\text{pv},k}]^T$ is the solar power boost converter state vector, $\chi_{3,k} = [\hat{U}_{\text{dcpv},k}\ \ \hat{I}_{\text{pv},k}]^T$ is the vector estimated by the neural identifier, $u_3 = u_{\text{pvbo},k}$ is the control vector, $\hat{y}_3 = [\hat{h}_{31}(x_{3,k})\ \ \hat{h}_{32}(x_{3,k})]^T = [\hat{U}_{\text{dcpv},k}\ \ \hat{I}_{\text{pv},k}]^T$ is the output vector to be controlled, and $\hat{f}_3(x_{3,k}) = [\hat{f}_{31}(x_{3,k})\ \ \hat{f}_{32}(x_{3,k})]^T$, where

$$\begin{aligned}\hat{f}_{31}(x_{3,k}) &= w_{11,k}S(U_{\text{dcpv},k}) + w_{12,k}S(I_{\text{pv},k})\\ &\quad + w_{13,k}S(U_{\text{dcpv},k})S(I_{\text{pv},k}) + \varpi_{3,1}\hat{I}_{\text{pv},k}\\ \hat{f}_{32}(x_{3,k}) &= w_{21,k}S(I_{\text{pv},k}) + w_{22,k}S(U_{\text{dcpv},k})\\ &\quad + w_{23,k}S(U_{\text{pv},k}) + w_{24,k}S(I_{\text{pv},k})S(U_{\text{dcpv},k})\end{aligned}$$

where $U_{\text{dcpv},k}$ is the boost output voltage $(V)$, $I_{\text{pv}}$ is the boost output current (in amperes), and $U_{\text{pv},k}$ is the output solar panel array voltage (in volts). Applying Theorem 1, the neural linearization control of the dc voltage is calculated as follows:

$$I_{\text{pvref},k} = \frac{-1}{\varpi_{3,1}}\hat{f}_{31}(x_{3,k}) + v_{3,1}. \tag{32}$$

The neural linearization control of the current is obtained as

$$u_{\text{pvbo}} = \frac{-1}{\varpi_{3,2}}\hat{f}_{32}(x_{3,k}) + v_{3,2}. \tag{33}$$

The decoupled control part for the dc voltage $v_{3,1}$ and current $v_{3,2}$ boost converter is defined as in Section II [see (12)–(17)], where the sliding surface of the boost converter dc voltage is defined as $s_{3n,1,k} = U_{\text{dcpvref},k} - \hat{U}_{\text{dcpv},k}$, and the sliding surface for the boost converter current is selected as $s_{3n,2,k} = I_{\text{pvref},k} - \hat{I}_{\text{pv},k}$.

*2) SPS Inverter:* The objective of this controller is to regulate the injected active and reactive power into the microgrid via control of the currents flow between the grid and the inverter. The proposed RHONN identifier is selected as follows:

$$\chi_{4,k+1} = \hat{f}_4(x_{4,k}) + \hat{B}_4 u_4(x_{4,k}) \tag{34}$$

$$\hat{y}_{4,k} == \hat{h}_4(x_{4,k}) \tag{35}$$

where $x_{4,k} = [i_{d,k} \;\; i_{q,k}]^T$ is the solar panel inverter state vector, $\chi_4 = [\hat{i}_{d,k} \;\; \hat{i}_{q,k}]^T$ is the vector estimated by the neural identifier, $u_{4,k} = [u_{d,k} \; u_{q,k}]^T$ is the control vector, $\hat{y}_4 = [\hat{h}_{41}(x_{4,k}) \;\; \hat{h}_{42}(x_{4,k})]^T = [\hat{i}_{d,k} \;\; \hat{i}_{q,k}]^T$ is the output vector to be controlled, $\hat{B}_4 = \text{diag}[\varpi_{4,1}, \varpi_{4,2}]$, and $\hat{f}_4(x_{4,k}) = [\hat{f}_{41}(x_{4,k}) \;\; \hat{f}_{42}(x_{4,k})]^T$, where

$$\hat{f}_{41}(x_{4,k}) = w_{11,k}S(i_{d,k}) + w_{12,k}S(i_{q,k}) + w_{13,k}S(i_{d,k})S(i_{d,k})$$

$$\hat{f}_{42}(x_{4,k}) = w_{21,k}S(i_{q,k}) + w_{22,k}S(i_{d,k}) + w_{23,k}S(i_{q,k})S(i_{d,k}).$$

Here, $i_{d,k}$ and $i_{q,k}$ are the grid $d$ and $q$ currents, respectively; $u_{d,k}$ and $u_{q,k}$ are the converter-side $d$ and $q$ voltages, respectively. Using Theorem 1, the neural linearization control of the grid currents is obtained as

$$\begin{bmatrix} u_d \\ u_q \end{bmatrix} = \hat{B}_4^{-1} \begin{bmatrix} -\hat{f}_{41}(x_{4,k}) \\ -\hat{f}_{42}(x_{4,k}) \end{bmatrix} + \begin{bmatrix} v_{4,1} \\ v_{4,2} \end{bmatrix} \tag{36}$$

where $v_{4,1}$ and $v_{4,2}$ are the grid currents of the decoupled controller, which are calculated following the controller design problem, as explained in Section II [see (12)–(17)]. The sliding surfaces for the grid *d*–*q* currents, $s_{4n,1,k}$ and $s_{4n,2,k}$, are defined as $s_{4n,1,k} = i_{\text{dref},k} - \hat{i}_{d,k}$ and $s_{4n,2,k} = i_{\text{qref},k} - \hat{i}_{q,k}$, respectively. The desired values of the grid currents are obtained by using a discrete-time PI controller, as in (28) and (29).

### C. BB Neural Controller

*1) Buck–Boost:* The control objective is to allow for charging and discharging operation modes (buck or boost mode). For the current flow direction between the converter and the battery, the positive sign means that the BB is discharging, while the negative sign means that it is charging. Taking into account the adaptive nature of the RHONN identifier, and the similitude between the buck and boost converter models, a single RHONN identifier is proposed for both cases as

$$\chi_{5,k+1} = \hat{f}_5(x_{5,k}) + \hat{B}_5 u_5(x_{5,k}, k) \tag{37}$$

$$\hat{y}_{5,k} == \hat{h}_5(x_{5,k}) \tag{38}$$

where $x_{5,k} = [U_{\text{dcbtt},k} \;\; I_{\text{btt},k}]^T$ is the buck–boost power converter state vector, $\chi_{5,k} = [\hat{U}_{\text{dcbtt},k} \;\; \hat{I}_{\text{btt},k}]^T$ is the vector estimated by the neural identifier, $u_5 = u_{c,k}$ is the input signal, $\hat{y}_5 = \hat{h}_{52}(x_{5,k}) = \hat{I}_{\text{btt},k}$ is the output to be controlled, $\hat{B}_5 = \text{diag}[0, \varpi_{5,2}]$, and $\hat{f}_5(x_{5,k}) = [\hat{f}_{51}(x_{5,k}) \;\; \hat{f}_{52}(x_{5,k})]^T$, where

$$\begin{aligned} \hat{f}_{51}(x_{5,k}) &= w_{11,k}S(U_{\text{dcbtt},k}) + w_{12,k}S(I_{\text{btt},k}) \\ &\quad + w_{13,k}S(U_{\text{dcbtt},k})S(I_{\text{btt},k}) + \varpi_{5,1} I_{\text{btt},k} \\ \hat{f}_{52}(x_{5,k}) &= w_{21,k}S(I_{\text{btt},k}) + w_{22,k}S(U_{\text{dcbtt},k}) \\ &\quad + w_{23,k}S(I_{\text{btt},k})S(U_{\text{dcbtt},k}) \end{aligned}$$

with $U_{\text{dcbtt},k}$ being the buck–boost output voltage (in volts), $I_{\text{btt}}$ the buck–boost output current (in amperes), and $U_{\text{btt},k}$ the BB voltage (in volts). The BB current reference is calculated as follows:

$$I_{\text{bttref},k} = \frac{P_{\text{bttref},k}}{U_{\text{dcbtt},k}} \tag{39}$$

where $P_{\text{bttref}}$ is the BB power reference. The neural linearization control part of the current flow through the buck–boost converter inductor is obtained as follows:

$$u_{c,k} = \frac{1}{\varpi_{5,2}} \left( -\hat{f}_{52}(x_{5,k}) \right) + v_5 \tag{40}$$

where $\varpi_{5,2} \neq 0$ is a fixed control weight and $v_5$ is the buck–boost converter output-current -decoupled control; its sliding surface is defined as $s_{5n,k} = I_{\text{bttref},k} - \hat{I}_{\text{btt},k}$.

*2) BB Inverter:* The control objective is divided as follows: 1) for the charging operation mode, the inverter controller objective is to maintain the dc-bus voltage constant, so the controller is the same as the one applied to the dc-link voltage at WPS, and 2) for the discharging operation mode, the purpose is to control the active and reactive power injected into the grid, so the controller is the same as the one used in the SPS inverter.

## V. REAL-TIME SIMULATION RESULTS

The proposed local controller, the microgrid, and the selected IEEE nine-bus network are simulated in real time using the SimPower System toolbox of MATLAB[1] and the Opal-RT (OP 5600) Simulator.[2] To determine the size of the WPS, the SPS, the BB, and the power converters, different factors are considered, as addressed in [28] and[29]. Considering that this article is focused on the resilience enhancement of the grid-connected microgrid, only the variability of renewable energy resources (wind speed and solar irradiation for the considered site) and the load demand are considered. The expected maximum power generated by the microgrid is 2.86%(10.5 MW) of the system total power. The maximum generated power by the WPS and SPS is 85% (9 MW) and 15% (1.5 MW) of the microgrid power, respectively. The BB is used to maximize the usage of the renewable energy and to minimize the power injection from the power system by storing energy whenever the supply from the WPS and SPS exceeds the load demand. The maximum power that can be injected to the microgrid is 500 kW. In addition, a resistive load with a value of 10 MW is installed in order to maintain a balanced power flow. Moreover, the microgrid design allows us to supply the power system by generated power from the DERs. Table I presents the

---

[1] MATLAB, Simulink. de 1994-2018, The Math Works, Inc.

[2] Opal-RT (OP5600) Simulator Opal-RT Technologies, Inc.

TABLE I
MICROGRID EQUIPMENT SIZING AND PARAMETERS

| DERs | Equipments | Parameters |
|---|---|---|
| WPS | Electric Size (Pwps, V, F) | 1.5 MW (6), 575 V, 60 Hz |
| | Turbine (wind, blade, inertia) | 15.5 m/s, 3, $10^3 kg.m^2$ |
| | DFIG Stator $R_s$, $L_s$, $L_m$ | $0.012\Omega$, $13.7mH$, $13mH$ |
| | DFIG Rotor $R_r$ , $L_r$ | $0.021\Omega$, $13.6mH$ |
| | Back-to-back (P, V, F) | $1.5MW$, $750VAC$, $60Hz$ |
| | DC-link $R_g$, $L_g$, $C$ | $0.3666\Omega$, $3.1mH$, $220\mu F$ |
| SPS | Electric Size ($P_{SPS}$, $V$, $F$) | $250KW(6)$ , $575V$, $60Hz$ |
| | PV (irr, $Vdc$, $Pdc$) | $10^3 W/m^2$, $481V$, $235KW$ |
| | SPS inverter line $R$, $L$ | $0.3666\Omega$, $0.76mH$ |
| | SPS boost $L_{pv}$, $C_{pv}$ | $0.76mH$, $470\mu F$ |
| | Inverter (P, V, F) | $500KW$, $750VAC$, $60Hz$ |
| | Boost (P, V, I) | $300KW_p$, $10^3 VDC$, $600A$ |
| BB | Electric Size ($P_{BB}$, V, F) | $500kW$, $575V$, $60Hz$ |
| | BB Buck-Boost $L_{btt}$, $C_{btt}$ | $0.76mH$, $470\mu F$ |
| | Buck boost (P,V, I) | $600KW_p$, $10^3 VDC$, $1145A$ |

TABLE II
IEEE NINE-BUS POWER GENERATION

| Bus | P (MW) | Q (Mvar) | Load (MW) | Load (Mvar) |
|---|---|---|---|---|
| 1 | 72.19 | 26.8 | 0 | 0 |
| 2 | 163 | 6.69 | 0 | 0 |
| 3 | 85 | -10.78 | 0 | 0 |
| 4 | 0 | 0 | 0 | 0 |
| 5 | 0 | 0 | 125 | 50 |
| 6 | 0 | 0 | 90 | 30 |
| 7 | 47 | 0 | 0 | 0 |
| 8 | 0 | 0 | 100 | 35 |
| 9 | 10.5 | 0 | 0 | 0 |

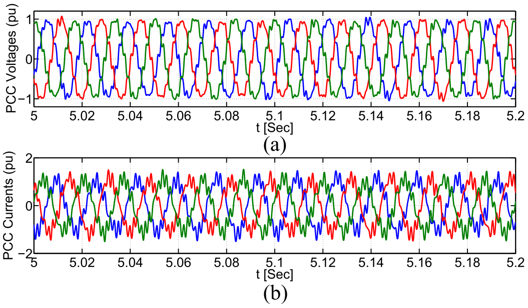

Fig. 3. Three-phase voltages and current: normal grid conditions.

parameters and the power equipment sizing of the microgrid under study. To evaluate the capabilities of the proposed DER local controllers in the presence of grid disturbances, different fault grid conditions are considered: single-phase-to-ground, two-phase-to-ground, and three-phase-to-ground, which are applied at two different locations. The first location is selected between buses six and nine (near to bus six, Fig. 2), whereas the second one is placed between the point of common coupling (PCC) bus and the microgrid. Table II displays the parameters of the power generations in each bus, including the microgrid (for more details about the IEEE nine-bus parameters, see [26] and [27]).

### A. Normal Grid Conditions

The objective of this experiment is to test the proposed local controller performances under ideal grid conditions. The control tracking results of DERs are presented in Figs. 3–11. The following microgrid operation conditions are considered.

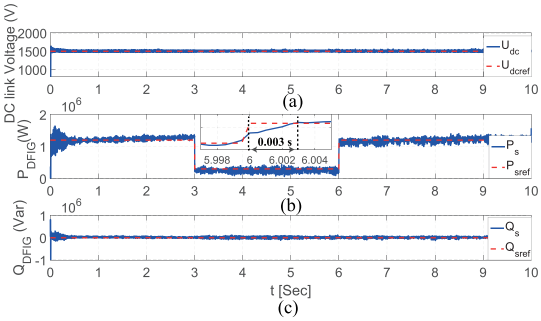

Fig. 4. WPS-controlled dynamics: NSML and normal grid conditions.

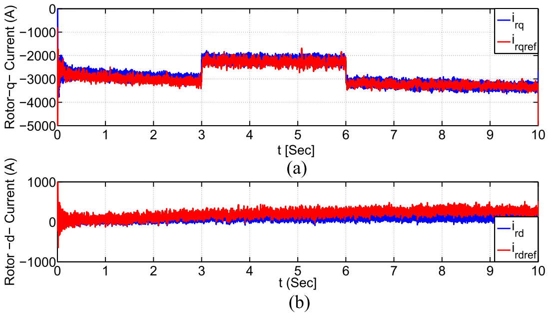

Fig. 5. DFIG $d$–$q$ rotor currents: NSML and normal grid conditions.

1) The generated active power from each DER is forced to track a time-varying trajectory in order to test the proposed control scheme in the presence of reference changes.
2) In real applications, these reference changes cause WPS and SPS power generation fluctuation due to fast wind speed and cloud transients.
3) The maximum power point tracking is not considered for any WPS or SPS.
4) The generated reactive power from each DER is kept at zero in order to ensure power factor equal to 1.
5) The load demand is fixed at 10 MW during the whole simulation lapse.
6) From $t = 0$ s to $t = 3$ s and $t = 6$ s to $t = 10$ s, the generated power from the microgrid satisfies the load demand, and the exceeded power is injected in the power system.
7) From $t = 3$ s to $t = 6$ s, the generated power from the microgrid is not enough to satisfy the load demand, and the power is injected from the power system.

Fig. 3(a) and (b) illustrates the three-phase voltages and the three-phase currents in per unit (p.u.), as measured at the PCC bus, respectively. Fig. 4(a) displays the dc voltage generated at the output of the dc link, while the stator active and reactive power obtained from the DFIG stator are presented in Fig. 4(b) and (c), respectively. The dc voltage is forced to track a constant value of 1.5 kV, whereas the stator active power is forced to track a time-varying reference, and the stator reactive power is fixed at zero. Fig. 5 displays the tracking response of the DFIG $d$–$q$ rotor currents. The rotor $q$ current tracks a time-varying reference obtained from the outer control loop of stator active power, and the rotor $d$ current is forced to be at a constant value defined from the reactive power outer control loop (see Section IV-A2).

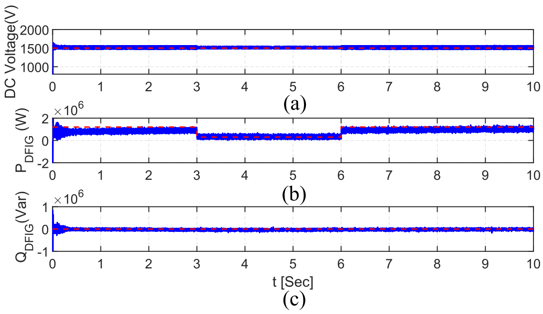

Fig. 6. WPS controlled dynamics: PI, normal grid conditions.

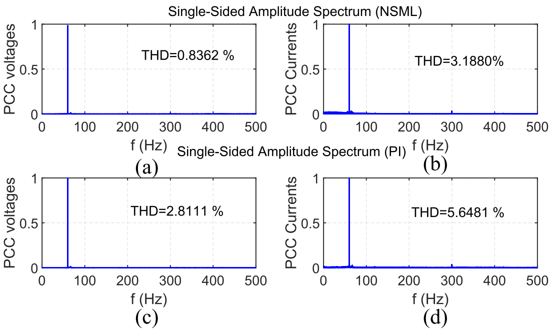

Fig. 7. THD for the NSML and the PI controllers.

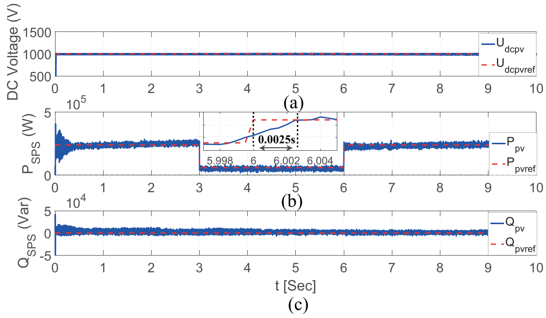

Fig. 8. Solar-panel-controlled dynamics: NSML and normal grid conditions.

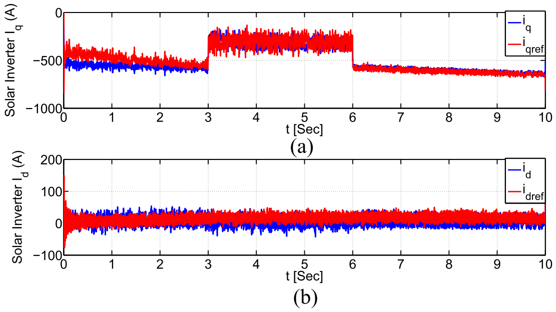

Fig. 9. Solar panel inverter $d$–$q$ currents: NSML and normal grid conditions.

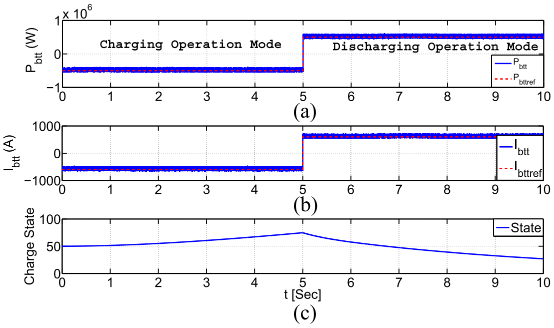

Fig. 10. BB charging and discharging operating modes.

The NSML controller is used for the inner control loop to force the rotor currents to track their desired references. In order to highlight the benefits of the proposed scheme for DER dynamics control, a comparison with the PI controller, which is the most used one, is done. As an example, it is used to control the WPS active and reactive power. Fig. 6 presents the obtained WPS dynamics when controlled by the PI scheme. Fig. 7 illustrates the single-side amplitude analyses and the total harmonic distortion (THD) of the voltages and currents, respectively, as measured at the PCC for the NSML (THD $= 0.8362\%$ [see Fig. 7(a)] and THD $= 3.1880\%$ [see Fig. 7(b)]) and for the PI (THD $= 2.8111\%$ [see Fig. 7(c)] and THD $= 5.6481\%$ [see Fig. 7(d)]) controllers. It is clear to see that both controllers achieve good WPS dynamics trajectory tracking with notable improvement in THD voltages and currents values at the PCC when the proposed scheme is utilized. In addition, the response time of the proposed controller is 0.003 s [see Fig. 4(b)], which ensures the WPS trajectory tracking even in the presence of power generation fluctuations caused by fast wind changes $(\geq 0.003\,\text{s})$. Fig. 8(a) portrays the dc voltage at the output of the solar panel boost converter, while Fig. 8(b) and (c) presents the solar panel inverter active and reactive power, respectively. The NSML controller is used to force the output of the boost converter to track a constant value of 1 kV, whereas the active power at the solar panel inverter is forced to track a time-varying reference, where its amplitude can vary from 125 to 250 kW. The solar panel inverter reactive power is maintained constant at zero. The nominal value of the generated power from the solar panels is 1.5 MW. The tracking response of the solar panel inverter $d$–$q$ currents is presented in Fig. 9, where the output of the active and reactive power PI controller is used to generate the inverter current desired dynamics (see Section IV-B2). From the obtained results, it is possible to conclude that the proposed controller for SPS ensures good trajectory tracking even in the presence of reference changes. In addition, the response time of the proposed controller is 0.0025 s [see Fig. 8(b)], which ensures SPS stability even in the presence of power generation fluctuations caused by fast cloud transients $(\geq 0.0025\,\text{s})$. Fig. 10(a) illustrates the direct power and Fig. 10(b) displays the direct current flow between the BB and the buck–boost converter for charging and discharging modes. The BB state of charge is presented in Fig. 10(c). In the charging operating mode, $t = 0$ to $t = 5$ s, the boost mode is selected. For this mode, a negative direct power desired value is applied, and (39) is used to calculate the desired trajectory of the direct current. In the discharging operating mode, $t = 5$ s to $t = 10$ s, the buck mode is chosen to obtain a positive direct power, and again, (39) is used to determine the reference of the direct current. Fig. 11(a) gives the dc voltage at the output of the

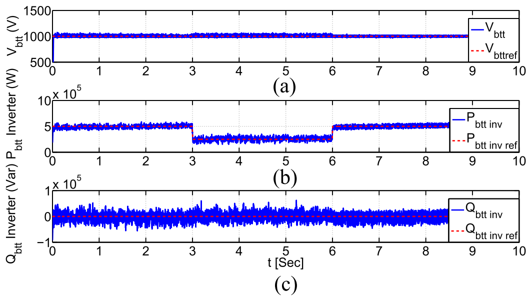

Fig. 11. BB-controlled dynamics: NSML and normal grid conditions.

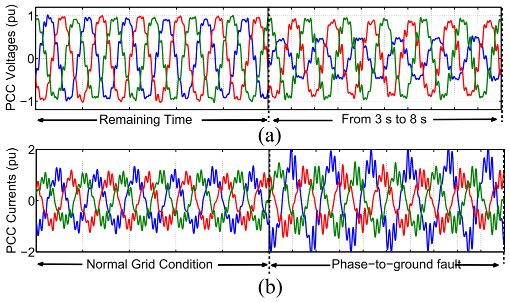

Fig. 12. Three-phase voltages and current: single-phase-to-ground fault.

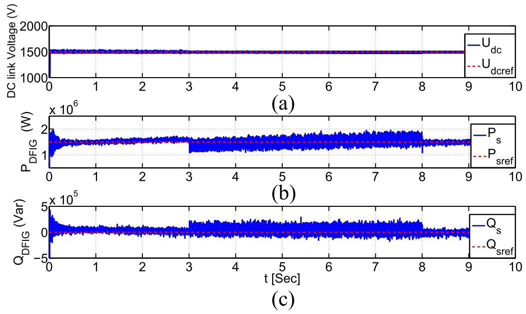

Fig. 13. WPS-controlled dynamics: NSML and single-phase-to-ground fault.

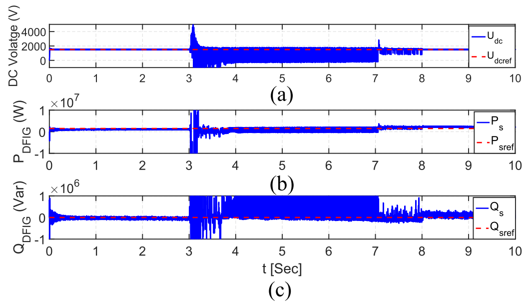

Fig. 14. WPS-controlled dynamics: PI and single-phase-to-ground fault.

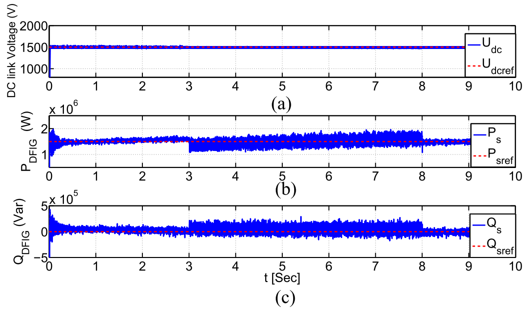

Fig. 15. SPS-controlled dynamics: NSML and single-phase-to-ground fault.

buck–boost converter in the discharging operating mode, which is forced by the buck converter controller to track a desired value equal to 1 kV. Fig. 11(b) and (c) displays the injected active and reactive power controlled by the BB inverter controller. The maximum power that can be injected to the grid from this system is 500 kW. From these results, it is very clear that the proposed local controller for each microgrid subsystem allows us to obtain tracking of the desired trajectories for the active and reactive powers, which are generated by the WPS, SPS, and BB, respectively, and ensures charging and discharging operation modes of the BB. In addition, the proposed control scheme improves the THD voltage and current value at the PCC in comparison with the PI controller.

### *B. Abnormal Grid Conditions: First Location*

In this section, single-phase-to-ground, two-phase-to-ground, and three-phase-to-ground grid faults are induced in bus six (see Fig. 2). These faults are applied for 5 s, which present enough time to examine the LVRT capacity of the installed DERs according to the standard IEEE 1159-1995.

*1) Single-Phase-to-Ground Fault Case:* Fig. 12(a) and (b) presents the three-phase voltages and the three-phase currents as obtained at the PCC, where a 50% voltage dip of 575 V appears at the faulted phase, and the other phases are kept at a nominal value. Fig. 13(a) displays the dc voltage at the output of the dc link, whereas the DFIG stator active and reactive powers, as generated by the WPS, are presented in Fig. 13(b) and (c), respectively. The stator active power reference is selected to be constant at 1.5 MW, and the stator reactive power set point is zero. Fig. 14 presents the WPS dynamics when the PI is used. It is clear that single-phase-to-ground fault causes high-amplitude ripples on the WPS dynamics when controlled by the PI scheme and may lead to instability of the isolated wind system and perhaps the microgrid. This fault has no significant impact on WPS dynamics when the proposed scheme is used. The solar panel dc voltage and the solar panel inverter active and reactive power responses are presented in Fig. 15(a)–(c), respectively. The injected active power generated by the solar panel is maintained at 250 kW, whereas the reactive power is kept constant at zero. Fig. 16 displays the dc voltage at the output of the BB buck–boost converter at the discharging operating mode and the BB inverter active and reactive power. The injected active power is operated to track a constant reference equal to 500 kW, while the reactive power is fixed at zero.

*2) Two-Phase-to-Ground Fault:* Fig. 17(a) and (b) illustrates the three-phase voltages and the three-phase currents as plotted at the PCC when a two-phase-to-ground fault is inserted. A 45% voltage dip of 575 V appears at the two faulted phases. The dc-link voltage and the DFIG stator active and reactive power

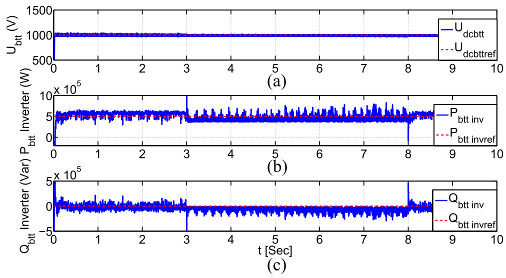

Fig. 16. BB-controlled dynamics: NSML and single-phase-to-ground fault.

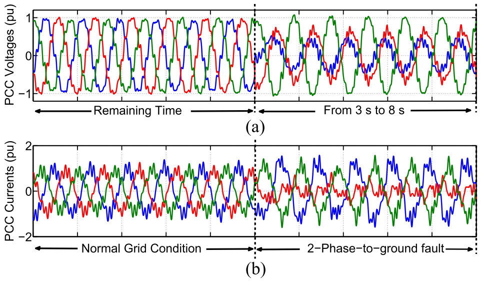

Fig. 17. Three-phase voltages and current: two-phase-to-ground fault.

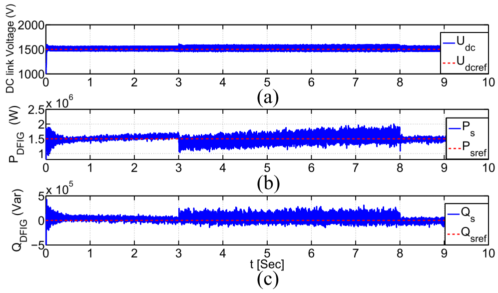

Fig. 18. WPS-controlled dynamics: NSML and two-phase-to-ground fault.

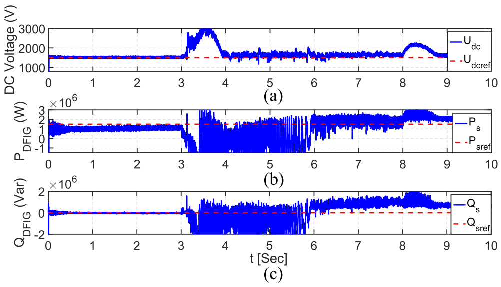

Fig. 19. WPS-controlled dynamics: PI and two-phase-to-ground fault.

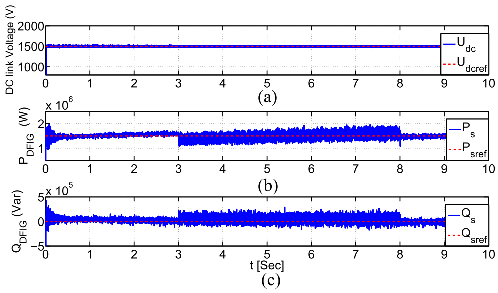

Fig. 20. SPS-controlled dynamics: NSML and two-phase-to-ground fault.

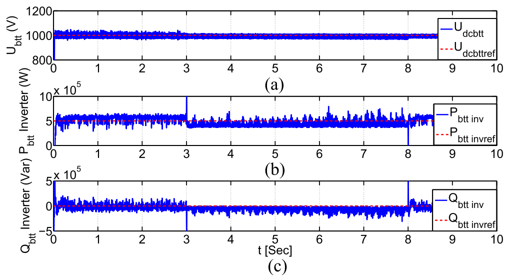

Fig. 21. BB-controlled dynamics: NSML and two-phase-to-ground fault.

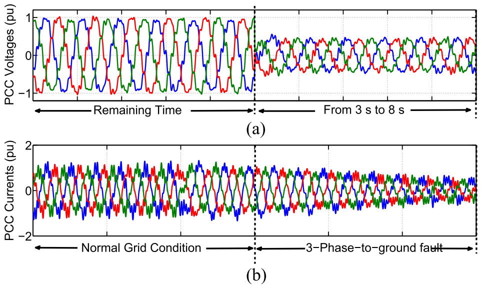

Fig. 22. Three-phase voltages and current: three-phase-to-ground fault.

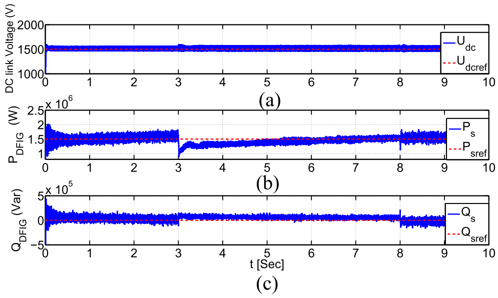

Fig. 23. WPS-controlled dynamics: NSML and three-phase-to-ground fault.

are presented in Fig. 18. Fig. 19 illustrates the WPS dynamics when the PI controller is used. From these results, it is clear that the proposed control scheme ensures stability of the WPS dynamics even in the presence of the two-phase-to-ground fault, while considerable ripples are presented when the PI controller is utilized. Fig. 20 displays the obtained result of the solar panel dynamics, such that the dc voltage at the output of the boost converter is presented in Fig. 20(a); the injected active and reactive powers at the output of the solar panel inverter are given in Fig. 20(b) and (c), respectively. The dc voltage at the output of the BB buck–boost converter and the active and reactive powers calculated at the output of the BB inverter are presented in Fig. 21(a)–(c), respectively.

*3) Three-Phase-to-Ground Fault:* Fig. 22(a) and (b) displays the dynamics of the three-phase voltage and the three-phase current at the PCC. A 50% symmetric voltage dip of 575 V appears. Fig. 23(a) presents the dc voltage at the output of the

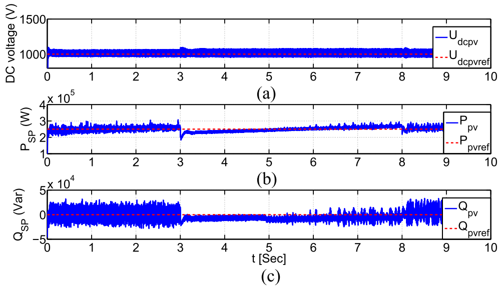

Fig. 24. SPS-controlled dynamics: three-phase-to-ground fault.

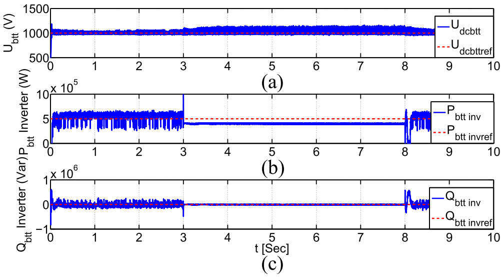

Fig. 25. BB-controlled dynamics: three-phase-to-ground fault.

dc link. The stator active and reactive powers when controlled by the proposed scheme and their references are illustrated in Fig. 23(b) and (c), respectively. Figs. 24 and 25 display the solar panel inverter and BB inverter controlled dynamics, respectively.

### *C. Abnormal Grid Conditions: Second Location*

For this second location, single-phase-to-ground and two-phase-to-ground faults are incepted between the PCC and the microgrid. The same results as for the first location case are obtained. The respective results are not included in order to fulfill the paper length requirements. From the results, we conclude that the proposed controller for each microgrid generation unit achieves the control objectives and ensures stability of the controlled system under normal and abnormal grid conditions. In addition, the LVRT capacity of the DERs is improved by using the proposed scheme as compared with the PI controller, which is unable to ensure stability in the presence of abnormal grid conditions.

## VI. CONCLUSION

This article presented a real-time simulation of an NSML controller for a grid-connected microgrid. The proposed local controller for each subsystem is used to control the active and reactive powers, which is injected to the grid. Each proposed local controller is based on an RHONN identifier. The neural identifiers approximate the respective nonlinear dynamics and allow the controller to reject disturbances caused by parameter variation and/or abnormal grid conditions. Real-time simulation results illustrate the effectiveness of the proposed scheme to achieve trajectory tracking of the DER power references even in the presence of grid disturbances. In addition, due to the fact that the identifier and the controller are separately designed for each component, new elements can be easily integrated for a large power system. Nevertheless, to select the neural identifier structure for each DER, to know an approximated mathematical model is helpful. In addition, only resistive load is considered in this article; however, various combinations of resistive, inductive, and capacitive loads could be considered. All these results allow us to establish that the proposed control schemes improve substantially the respective microgrid resilience. As a future work, the proposed control scheme can be extended to regulate the generated power of other distributed resources. In addition, it is advisable to include tests for a more complex power system with different grid fault scenarios.

## APPENDIX
## PROOF OF THEOREM 1

The DTSMC $v(x_k)$ is selected as (13). Taking into account the separation principle [23], the convergence proof of the proposed control scheme is analyzed as follows.

Due to identification error boundedness, there exists a bounded vector valued function$\Delta_{i,k}$; then, we have

$$x_k = \chi_k - \Delta_{i,k}, \quad i = 1, \dots, r \tag{41}$$

where $\|\Delta_{i,k}\| \leq \gamma_i, \gamma_i > 0$, and $r$ is the number of the state. The sliding surface at $k+1$ is defined using $x_k$ as follows:

$$s_{n,k+1} = x_{\text{ref},k+1} - x_{k+1}. \tag{42}$$

Using (41) in (42), we obtain

$$s_{n,k+1} = x_{\text{ref},k+1} - \chi_{k+1} + \Delta_{i,k}. \tag{43}$$

Using the neural linearization control (10), the sliding surface is expressed as follows:

$$s_{n,k+1} = x_{\text{ref},k+1} - v(x_k) + \Delta_{i,k}. \tag{44}$$

The DTSMC in (13) includes the following two cases.

1) For $||v_c(x_k)|| \leq u_0$, the control law $v_{c,k}$ is applied. Using (16) and (17) in (43), the sliding surface at $k+1$ is

$$s_{n,k+1} = k_n s_{n,k} + \Delta_{i,k}. \tag{45}$$

Let us define the Lyapunov function candidate $V_k = s_{n,k}^T s_{n,k}$; then, its difference is given as

$$\begin{aligned} \Delta V_k &= s_{n,k+1}^T s_{n,k+1} - s_{n,k}^T s_{n,k} \\ &= (k_n s_{n,k} + \Delta_{i,k})^T (k_n s_{n,k} + \Delta_{i,k}) - s_{n,k}^T s_{n,k} \\ &\leq (\|k_n\| \, \|s_{n,k}\| + \|\Delta_{i,k}\|)^2 - \|s_{n,k}\|^2 \\ &\leq (\|k_n\| \, \|s_{n,k}\| + \gamma_i)^2 - \|s_{n,k}\|^2 \\ &\leq \; - (1-\theta_1)\eta_1 \, \|s_{n,k}\|^2 + \gamma_i^2 \\ &\quad + (-\theta_1 \eta_1 \, \|s_{n,k}\| + 2 \, \|k_n\| \, \gamma_i) \, \|s_{n,k}\| \end{aligned}$$

with $0 < \theta_1 < 1$, $\eta_1 = (1 - \|k_n\|^2)$, and $\eta_1 > 0$, and for the region $\|s_{n,k}\| \geq \frac{2\gamma_i \|k_n\|}{\theta_1 \eta_1}$, we obtain

$$\begin{aligned} \Delta V_k &\leq \; -(1-\theta_1)\eta_1 \, \|s_{n,k}\|^2 + \gamma_i^2 \\ \Delta V_k &\leq \; -(1-\theta_2)\beta_1 \, \|s_{n,k}\|^2 - \theta_2 \beta \, \|s_{n,k}\|^2 + \Gamma^2 \\ \Delta V_k &\leq \; -(1-\theta_2)\beta_1 \, \|s_{n,k}\|^2 \end{aligned}$$

with $0 < \theta_2 < 1, \beta_1 = (1 - \theta_1)\eta_1$ and $\beta_1 > 0$. Therefore, $\Delta V_k \leq 0,\ \forall \|s_{n,k}\| \geq \sqrt{\frac{\gamma_i^2}{\theta_2 \beta_1}}$, and the solution of system (43) is ultimately bounded.

2) For $\|v_c(x_k)\| > u_0$, the control law $u_0 \frac{v_{\text{eqn}}(x_k)}{\|v_{\text{eqn}}(x_k)\|}$ is utilized.

Let us define the equivalent control by imposing $s_{n,k} - x_{\text{ref},k} + \chi_k = 0$. The equivalent control is defined as

$$v_{\text{eqn},k} = s_{n,k} + f_{n,k} \tag{46}$$

with $f_{n,k} = -x_{\text{ref},k} + \chi_k + x_{\text{ref},k+1}$. Then, the expression of the sliding-mode surface is

$$\begin{aligned} s_{n,k+1} &= s_{n,k} - x_{\text{ref},k} + x_k + x_{\text{ref},k+1} - v_n(x_k) + \Delta_{i,k} \\ &= (s_{n,k} + f_{n,k}) \left(1 - u_0 \frac{1}{\|v_{\text{eqn},k}\|}\right) + \Delta_{i,k} \end{aligned}$$

Using the Lyapunov function candidate $V_k = s_{n,k}^T s_{n,k}$, we have

$$\begin{aligned} \Delta V_k &= s_{n,k+1}^T s_{n,k+1} - s_{n,k}^T s_{n,k} \\ &\leq (\|s_{n,k} + f_{n,k}\| - \|u_0\| + \|\Delta_{i,k}\|)^2 - \|s_{n,k}\|^2 . \end{aligned}$$

Suppose that the control law $\|u(x_k)\| \leq u_0$ may vary within the domain [30], $\|f_{n,k} + \Delta_{i,k}\| \leq u_0$, and $\sigma < u_0$, where $\sigma = \|f_{n,k} + \Delta_{i,k}\|$; then, we have

$$\begin{aligned} \Delta V_k &\leq (\|s_{n,k}\| + \sigma - \|u_0\|)^2 - \|s_{n,k}\|^2 \\ &\leq (2\|s_{n,k}\| + \sigma - \|u_0\|)(\sigma - \|u_0\|) \\ &\leq -(2\|s_{n,k}\| + \sigma - \|u_0\|)(\|u_0\| - \sigma) . \end{aligned} \tag{47}$$

If $\|f_{n,k} + \Delta_{i,k}\| \leq \|u_0\| \leq (2\|s_{n,k}\| + \|f_{n,k} + \Delta_{i,k}\|)$ holds, then $\Delta V_k \leq 0$ [17]. Hence, $\|s_{n,k}\|$ and $\|v_{\text{eqn},k}\|$ both decrease monotonically. Therefore, there will be a time $k_1$ such that $\|v_{\text{eqn},k}\| \leq \|u_0\|$ for $k \geq k_1$. At that time, the control law $v_c$ is applied, yielding that the solution of the system (45) is ultimately bounded. □

## REFERENCES

[1] I. Sadeghkhani, M. E. Golshan, A. Mehrizi-Sani, and J. M. Guerrero, "Low-voltage ride-through of a droop-based three-phase four-wire grid-connected microgrid," *IET Gener., Transmiss. Distrib.*, vol. 12, no. 8, pp. 1906–1914, 2018.

[2] M. Yazdanian and A. Mehrizi-Sani, "Distributed control techniques in microgrids," *IEEE Trans. Smart Grid*, vol. 5, no. 6, pp. 2901–2909, Nov. 2014.

[3] M. J. Morshed and A. Fekih, "A fault-tolerant control paradigm for microgrid-connected wind energy systems," *IEEE Syst. J.*, vol. 12, no. 1, pp. 360–372, Mar. 2018.

[4] M. Nasiri, J. Milimonfared, and S. Fathi, "A review of low-voltage ride-through enhancement methods for permanent magnet synchronous generator based wind turbines," *Renew. Sustain. Energy Rev.*, vol. 47, pp. 399–415, Jul. 2015.

[5] K. Ma, W. Chen, M. Liserre, and F. Blaabjerg, "Power controllability of a three-phase converter with an unbalanced ac source," *IEEE Trans. Power Electron.*, vol. 30, no. 3, pp. 1591–1604, Mar. 2015.

[6] I. Ngamroo and T. Karaipoom, "Improving low-voltage ride-through performance and alleviating power fluctuation of DFIG WT in dc microgrid by optimal SMES with fault current limiting function," *IEEE Trans. Appl. Supercond.*, vol. 24, no. 5, 2014, Art. no. 5700805.

[7] S. Gkavanoudis and C. Demoulias, "Control strategy for enhancing the fault ride-through capability of a microgrid during balanced and unbalanced grid voltage sags," *Sustain. Energy, Grids Netw.*, vol. 3, pp. 1–11, 2015.

[8] Y. Soe, S. Aung, and Z. Linn, "Analysis on performance of dc micro-grid under fault condition," *Amer. Sci. Res. J. Eng. Technol., Sci.*, vol. 26, no. 3, pp. 1–12, 2016.

[9] R. Cardenas, M. Diaz, F. Rojas, J. Clare, and P. Wheeler, "Resonant control system for low-voltage ride-through in wind energy conversion systems," *IET Power Electron.*, vol. 9, no. 6, pp. 1297–1305, 2016.

[10] L. Shang and J. Hu, "Sliding-mode-based direct power control of grid-connected wind-turbine-driven doubly fed induction generators under unbalanced grid voltage conditions," *IEEE Trans. Energy Convers.*, vol. 27, no. 2, pp. 362–373, Jun. 2012.

[11] F. Ornelas-Tellez, J. J. Rico-Melgoza, E. Espinosa-Juarez, and E. N. Sanchez, "Optimal and robust control in dc microgrids," *IEEE Trans. Smart Grid*, vol. 9, no. 6, pp. 5543–5553, Nov. 2018.

[12] A. Bidram, F. L. Lewis, and A. Davoudi, "Distributed control systems for small-scale power networks: Using multiagent cooperative control theory," *IEEE Control Syst. Mag.*, vol. 34, no. 6, pp. 56–77, Dec. 2014.

[13] J. A. P. Lopes, C. L. Moreira, and A. G. Madureira, "Defining control strategies for microgrids in islanded operation," *IEEE Trans. Power Syst.*, vol. 21, no. 2, pp. 916–924, May 2006.

[14] W. G. Lee, T. T. Nguyen, H. J. Yoo, and H. M. Kim, "Low-voltage ride-through operation of grid-connected microgrid using consensus-based distributed control," *Energies*, vol. 11, no. 11, 2018, Art. no. 2867.

[15] N. Hatziargyriou, *Microgrids Architectures and Control*. Chichester, U.K.: Wiley, 2009.

[16] G. Rovithakis and M. Chistodoulou, *Adaptive Control with Recurrent High Order Neural Networks*. Berlin, Germany: Springer, 2012.

[17] E. N. Sanchez, A. Y. Alanis, and A. G. Loukianov, *Discrete-Time High Order Neural Control: Trained with Kalman Filtering*. Berlin, Germany: Springer, 2008.

[18] X. Zheng and X. Chen, "Enhancement on transient stability of LVRT of DFIG based on neural network d-STATCOM and crowbar," in *Proc. 11th IEEE Int. Conf. Anti-Counterfeiting, Sec., Identif.*, Xiamen, China, Oct. 27–29, 2017, pp. 64–68.

[19] A. S. Saidi and W. Helmy, "Artificial neural network-aided technique for low voltage ride-through wind turbines for controlling the dynamic behavior under different load conditions," *Wind Eng.*, vol. 43, no. 4, pp. 420–440, 2019.

[20] F. J. Lin, K. C. Lu, T. H. Ke, B. H. Yang, and Y. R. Chang, "Reactive power control of three-phase grid-connected PV system during grid faults using Takagi-Sugeno-Kang probabilistic fuzzy neural network control," *IEEE Trans. Ind. Electron.*, vol. 62, no. 9, pp. 5516–5528, Sep. 2015.

[21] A. Adounia, D. Chariaga, D. Diallob, M. B. Hameda, and L. Sbita, "FDI based on artificial neural network for low-voltage-ride-through in DFIG-based wind turbine," *ISA Trans.*, vol. 64, pp. 353–364, 2016.

[22] L. Djilali, E. N. Sanches, F. Ornelas-Tellez, and M. Belkheiri, "Neural network based controller for an ac microgrid connected to a utility grid," in *Proc. IEEE Latin Amer. Conf. Comput. Intell.*, Guadalajara, Mexico, Nov. 7–8, 2018, pp. 1–6.

[23] W. Lin and C. I. Byrnes, "Design of discrete-time nonlinear control systems via smooth feedback," *IEEE Trans. Autom. Control*, vol. 39, no. 11, pp. 2340–2346, Nov. 1994.

[24] V. Utkin, J. Guldner, and J. Shi, *Sliding Mode Control in Electro-Mechanical System*. Boca Raton, FL, USA: CRC Press, 2009.

[25] A. Varga, "A Schur method for pole assignment," *IEEE Trans. Autom. Control*, vol. AC-26, no. 2, pp. 517–519, Apr. 1981.

[26] The Illinois Center for a Smarter Electric Grid (ICSEG), "WSCC 9-Bus System," Power Cases. [Online]. Available: http://publish.illinois.edu/smartergrid/wscc-9-bus-system/, Accessed: Apr. 11, 2015.

[27] R. Kaur and D. Kumar, "Transient stability improvement of IEEE 9 bus system using power world simulator," *Int. J. Eng. Res. Appl.*, vol. 6, no. 1, pp. 35–39, 2016.

[28] I. Zenginis, J. S. Vardakas, J. Abadal, C. Vardakas, M. M. Guell, and C.Verikoukis,"Optimal power equipment sizing and management for cooperative buildings in microgrids," *IEEE Trans. Ind. Inform.*, vol. 15, no. 1, pp. 185–172, Jan. 2019.

[29] R. Atia and N. Yamada, "Sizing and analysis of renewable energy and battery systems in residential microgrids," *IEEE Trans. Smart Grid*, vol. 7, no. 1, pp. 1204–1213, May 2016.

[30] G. Bartolini, A. Ferrara, and V. I. Utkin, "Adaptive sliding mode control discrete-time system," *Automatica*, vol. 31, no. 5, pp. 769–773, 1995.